Effect of Tannic Acid on Photocatalytic Efficiency of $NiFe_2O_4$ and ZnO

Keziban Atacan*

Sakarya University, Biomedical, Magnetic and Semiconductor Materials Application and Research Center (BIMAS-RC), 54187 Sakarya, Turkey
*kezibanatacan@sakarya.edu.tr

Received: 03 August 2018
Accepted: 20 September 2018
DOI: 10.18466/cbayarfbe.450816

Abstract

ZnO, $NiFe_2O_4$, $NiFe_2O_4$/TA and $NiFe_2O_4$/TA/ZnO photocatalyts were successfully synthesized and characterized, and they demonstrated significant photocatalytic efficiency under visible-light. The photodegradation rates of congo red (CR) are 35.7%, 19.4%, 25.5% and 91.1% over the ZnO, $NiFe_2O_4$, $NiFe_2O_4$/TA and $NiFe_2O_4$/TA/ZnO for 180 min, respectively. The results display that the $NiFe_2O_4$/TA/ZnO has the most excellent photocatalytic efficiency for CR among to the other photocatalysts. Furthermore, $NiFe_2O_4$/TA/ZnO may be separated easily from solution by magnet because of the magnetic property of $NiFe_2O_4$. The considerable increment in efficiency of $NiFe_2O_4$/TA/ZnO can be attributed to synergistic effects between $NiFe_2O_4$, the tannic acid (TA) and ZnO, which extend lifetime and hinder the recombination of photogenerated charge carriers. This work presents new perspectives on the use of tannic acid based magnetic photocatalysts in wastewater treatment.

Keywords: $NiFe_2O_4$, tannic acid, magnetic separation, photocatalytic efficiency.

1. Introduction

Visible driven photocatalysis applied by preparing new functional materials presents new insights for wastewater treatment [1–3]. Semiconductor photocatalyts have an important potential due to it transform solar energy to chemical energy in the enviromental treatment [4]. ZnO, which only absorb the light in the UV range, is one of the influent photocatalysts, because of its wide band gap energy. The strategies such as doping with noble metals and coupling of other semiconductors have been developed to activate ZnO in visible region [5–7].

After photocatalytic processes, recycling and reuse of photocatalysts are of considerable significance for the maintainable use of resources [8,9]. Recently, magnetic semiconductors such as MFe_2O_4 (M=Cu, Zn, Co, Ni) have drawn attention about recycling and reuse of photocatalyts [8]. $NiFe_2O_4$ is a magnetic material with narrow band gap energy, high magnetic separation and chemical stability [4,10]. However pure $NiFe_2O_4$ illustrates weak photocatalytic performance owing to the rapid recombination of charge carriers [10]. When their own features of ZnO and $NiFe_2O_4$ are taken in consideration, the combination of ZnO and $NiFe_2O_4$ may overcome the above mentioned problems [10,11].

Tannic acid is the form of gallotannine, which is an ester of glucose and gallic acid [12]. Nuray et al., reported that the tannin is a suitable support material for photocatalysis. Units of phenolic groups of tannic acid may interact with photoinduced electrons. Then, the electron continues to the ester ring owing to the pi bonds in the tannic acid and the unpaired electrons over the oxygen. And finally, it leaves without splitting the ester ring. Tannic acid acts as electron scavengers in photocatalysis, delaying the recombination of the charge carriers [13].

Recently, many studies have been performed with ZnO/$NiFe_2O_4$ magnetic nanoparticles under visible light. However, no study has been published on the enhancing influence of the tannic acid as a modifier on photocatalytic activity of $NiFe_2O_4$/TA/ZnO. This study reports the preparation of magnetically separable $NiFe_2O_4$/TA/ZnO photocatalysts via solvothermal process and their photocatalytic efficiency for congo red (CR) decomposition. The $NiFe_2O_4$/TA/ZnO photocatalyst shows higher activity than ZnO and $NiFe_2O_4$. Under visible-light, neither ZnO alone nor $NiFe_2O_4$ alone is not photocatalytically active. In conclusion, this study is attributed to two basic topics. They are the synthesis of visible active $NiFe_2O_4$/ZnO and the delaying of recombination via TA.

2. Materials and Methods

2.1 Materials and apparatus

Zinc nitrate hexahydrate ($Zn(NO_3)_2 \cdot 6H_2O$, Merck), Nickel(II) Chloride Hexahydrate, ($NiCl_2 \cdot 6H_2O$, Merck), sodium hydroxide (NaOH, Merck), Iron(III) chloride hexahydrate ($FeCl_3.6H_2O$, Merck), ethylene glycol ($C_2H_6O_2$, TEKKİM), CR (commercial grade), and ethanol (Merck) were supplied.

2.2 Synthesis of photocatalysts

ZnO was synthesized by the method described in the work of Nuray et al. [14,15].

For synthesis of $NiFe_2O_4$ was used by solvothermal approach. In this procedure, 2 mmol $FeCl_3.6H_2O$ and 1 mmol $NiCl_2{\cdot}6H_2O$ were dissolved in $C_2H_6O_2$. Then, 15 mmol sodium acetate was added to the suspension and ultrasonicated for 1 h. Then, the solution heated at 160 °C for 18 h. The acquired $NiFe_2O_4$ was washed, and afterwards, separated by a magnet and dried at 70 °C.

In the preparation of $NiFe_2O_4$/TA, 0.5 g of $NiFe_2O_4$ nanoparticles were dispersed in 20 mL of water under ultrasonic stirring for 1 h. Subsequently, 0.25 g tannic acid was added to $NiFe_2O_4$ dispersion and stirred ultrasonically for 2 h. The obtained $NiFe_2O_4$/TA was separated with a magnet, and washed. Consequently, the nanocomposites were dried at 70 °C [16].

$NiFe_2O_4$/TA/ZnO was prepared by a microwave-hydrothermal method. Firstly, 0.1 g $NiFe_2O_4$/TA was sonicated 30 mL of DW and 4 mmol $Zn(NO_3)_2.6H_2O$ was added into the dispersion. After that, 12.5 mmol NaOH was dropped into the dispersion and stirred 1 h. The formed suspension was treated at 170 °C for 10 min in a microwave oven. The resulting samples washed and dried at 70 °C [13].

2.3 Instrumentation

The molecular structures of nanophotocatalyts were verified by powder X-ray diffraction (XRD, PAN-alytical Empyrean, Netherlands). The morphologies of samples were examined by using a scanning electron microscopy (SEM, Philips XL30 SFEG). The spectral characterizations were recorded via Fourier transform infrared Shimadzu UATR Two instrument (Japan). The optical features of products were determined by a UV-visible spectrophotometer (UV-Vis, Shimadzu UV-2600PC).

2.4 Photocatalytic testing

Photocatalytic efficiency of samples were determined by decomposition of CR. Irradiation was supplied by a 128 W visible light. In degradation procesess, 50 mg of nanophotocatalyst was dispersed by a stirrer in 16 ppm CR solution. Before illumination, the solutions were stirred for 30 min in the darkness to provide formation of adsorption/desorption equilibrium of CR. 5 mL of the aliquots were withdrawn at specific time intervals, separated and investigated by the UV–Vis spectroscopy in the maximum absorbance of CR. The rate of degradation was detected by the Equation (2.1): [13–15,17,18].

$$\text{degradation (\%)} = \frac{C_0\text{-}C}{C_0} \text{ x } 100 \qquad (2.1)$$

where C_0 and C demonstrate the initial and the reaction concentrations of CR.

3. Results and Discussion

3.1 Characterization of photocatalysts

Figure 1 displays the XRD profiles of the nanophotocatalyts. The XRD profile of ZnO demonstrates apparent peaks for hexagonal ZnO (JCPDS no.79-0206). The peak values at 2θ values of 31.7, 34.4, 36.2, 47.5, 56.6, 62.9, 66.4, 67.9, 69.1, 72.6, 76.9, 81.4, 89.6° are indexed as (100), (002), (101), (102), (110), (103), (200), (112), (201) and (004) planes of the ZnO with hexagonal wurtzite structure (ICSD98-015-5780), respectively. The diffraction peaks at the 2θ values of 30.26, 35.64, 43.30, 53.83, 57.26 and 62.89° are related to (220), (311), (400), (422), (511) and (440) planes of spinel $NiFe_2O_4$ (JCPDS no. 54-0964), respectively. In the XRD spectra of $NiFe_2O_4$/TA, $NiFe_2O_4$ are shadowed by modifiying TA, leading to the invisible of the some of the peaks of TA caused to disappear some of the $NiFe_2O_4$ peaks. In the XRD spectra of $NiFe_2O_4$/TA/ZnO, both $NiFe_2O_4$ and TA peaks are observed. This situation is evidence that the composite is formed [13–15,17–19].

The morphology of the products has been verified by SEM analysis. Figure 2a-d illustrates the SEM images of ZnO, $NiFe_2O_4$, $NiFe_2O_4$/TA and $NiFe_2O_4$/TA/ZnO. As can be seen Figure 2a, ZnO has irregular nanoplate structures [14,18]. $NiFe_2O_4$ consists of lots of agglomerated spherical nanoparticles (Figure 2b) [10]. In Figure 2c, Tannic acid can not be observed because the surface of the TA molecule is completely covered with aglomere $NiFe_2O_4$ nanoparticles. Figure 2d shows $NiFe_2O_4$/TA/ZnO nanostructures containing ZnO nanoplates and agglomerated spherical $NiFe_2O_4$ nanoparticles.

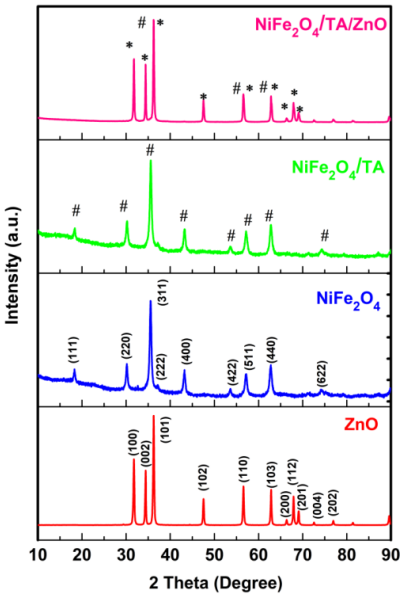

Figure 1. XRD patterns of the photocatalyts.

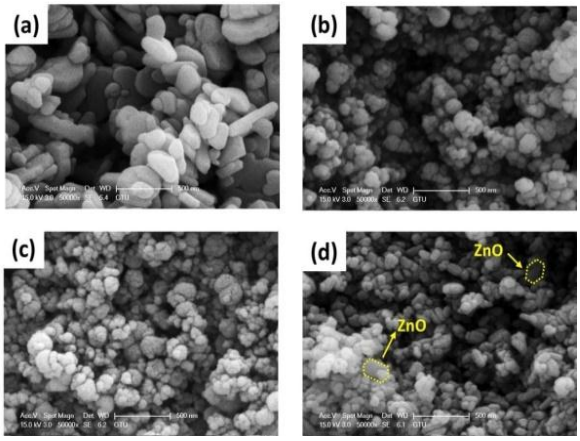

Figure 2. SEM images of (a) ZnO, (b) $NiFe_2O_4$, (c) $NiFe_2O_4$/TA and (d) $NiFe_2O_4$/TA/ZnO.

The optical features of the photocatalyts were examined by UV-visible diffuse reflectance spectra and band gap energies of them were displayed in Figure 3. As shown in Figure 3, the band gap energies of ZnO, $NiFe_2O_4$, $NiFe_2O_4$/TA and $NiFe_2O_4$/TA/ZnO correspond to visible region. With modifiying TA and ZnO, band gap energy of $NiFe_2O_4$ is replacing to the left. UV-DRS datas are described the Kulbelka-Munk (K-M) relation $(F(R)=(1-R)^2/2R$. In here, R is the is the reflection of the product [15]. The band gap energies of ZnO, $NiFe_2O_4$, $NiFe_2O_4$/TA and $NiFe_2O_4$/TA/ZnO are detected 3.24 eV, 1.88 eV, 2.13 eV and 2.63 eV, respectively.

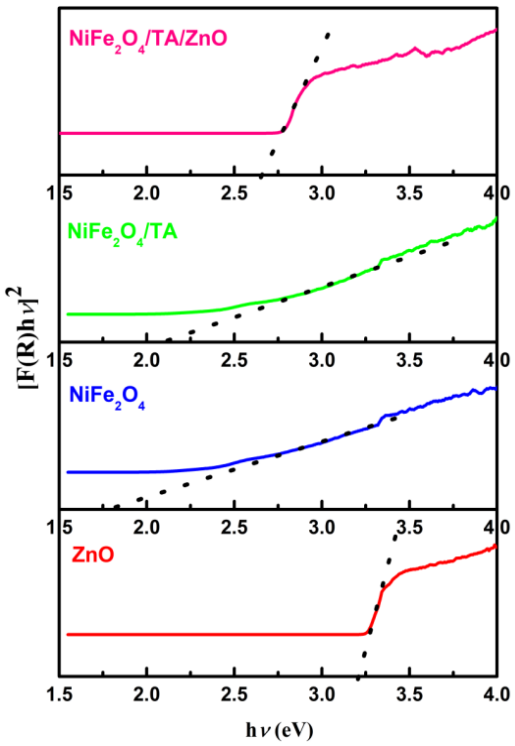

Figure 3. The K-M function versus hν curves of the products for band gap energy detection.

FT-IR spectra of the products are demonstrated in Figure 4. The band at 440 cm^{-1} corresponds to Zn-O stretching vibrations (Figure 4a). As can be illustrated in Figure 4b-d, the peaks at 580 cm^{-1} and 440 cm^{-1} exhibit Fe-O and Ni-O bond, respectively. The peaks around 1626-1440 cm^{-1}, 1200 and 1050 cm^{-1} are imputed to C=C− C vibrations in the aromatic carbon, C–OH stretching vibrations and C–O vibrations in the epoxy groups for tannic acid, respectively [20]. The peak at 3435 cm^{-1} correnponds to -OH vibrations of the water molecule [20].

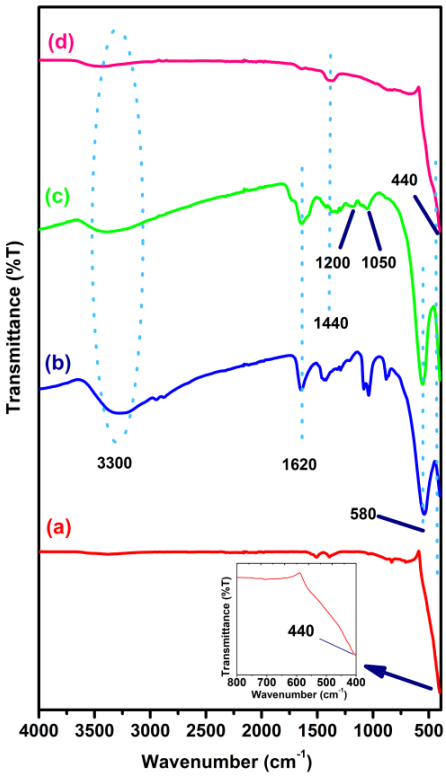

Figure 4. FT-IR spectra of (a) ZnO, (b) $NiFe_2O_4$, (c) $NiFe_2O_4$/TA and (d) $NiFe_2O_4$/TA/ZnO.

3.2 Photocatalytic testing

The photocatalytic efficiency of products have been examined via the CR degradation under visible light and the results are exhibited in Figure 5. As can be illustrated in Figure 5a, the degradation rates of ZnO, $NiFe_2O_4$, $NiFe_2O_4$/TA and $NiFe_2O_4$/TA/ZnO, 35.7%, 19.4%, 25.5% and 91.1%, respectively, within 180 min. When the photocatalytic efficiencies of of ZnO, $NiFe_2O_4$ and $NiFe_2O_4$/TA are compared, it is observed that TA is an enhancing effect on the performance of $NiFe_2O_4$. The results demonstrated that $NiFe_2O_4$/TA/ZnO exhibited much superior photocatalytic efficiency than ZnO, $NiFe_2O_4$ and $NiFe_2O_4$/TA. $NiFe_2O_4$ displays weak photocatalytic efficiency owing to rapid recombination of charge carriers. Since band gap energy of ZnO is wide, it is not very active in visible region. With TA modification, efficiency of $NiFe_2O_4$ has been enhanced. To determine the reaction kinetics of the degradation of CR on photocatalysts, the apparent rate constants were calculated by the pseudo-first-order kinetics [4,19].

$$\ln(C_0/C)=kt \quad (3.1)$$

where k represents for the first-order rate constant. From the Figure 5b, determined the rate constants of photocatalyts are shown in Table 1. When the K values of products are compared, $NiFe_2O_4$/TA/ZnO exhibited the higher degradation rate constant than the others.

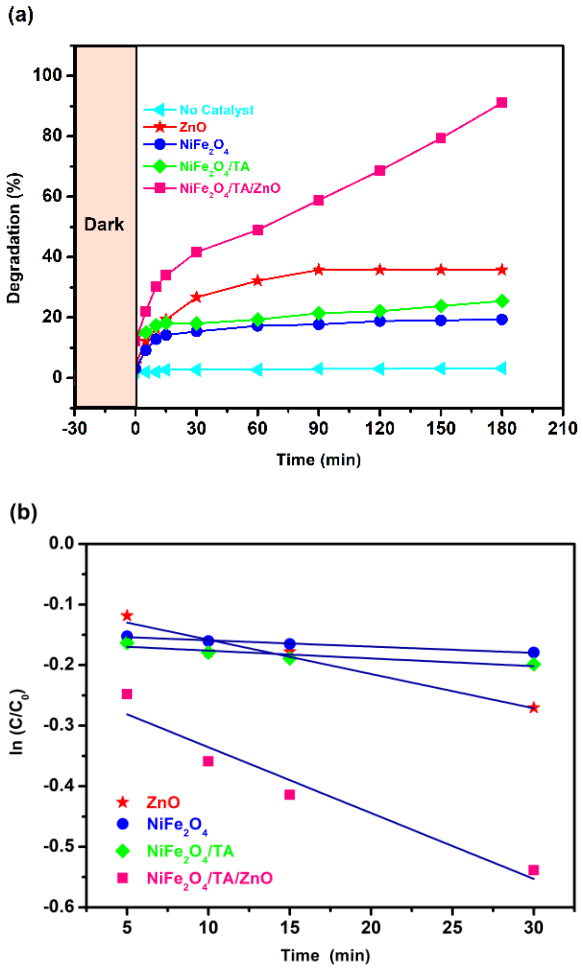

Figure 5. (a) The photodegradation of CR in existence of different nanophotocatalysts. (b) First order kinetics.

Table 1. k values of CR photodegradation in the existence of the samples.

Samples	k (min^{-1})
ZnO	$5.66x10^{-3}$
$NiFe_2O_4$	$1.04x10^{-3}$
$NiFe_2O_4$/TA	$1.28x10^{-3}$
$NiFe_2O_4$/TA/ZnO	$10.8x10^{-3}$

Thanks to the molecular structure of tannic acid, phenolic groups may interact with photoinduced electrons and then the unpaired electrons in phenolic groups are delocalized over the aromatic ring, this results in resonance formation. Thus, TA acts as an electron capture. Since the electrons amassed on the CB of $NiFe_2O_4$ transfer to TA, recombination of charge carriers are greatly inhibited [13].

3.3. Photocatalytic mechanism

According the photodegradation datas, suggested a photocatalysis mechanism of $NiFe_2O_4$/TA/ZnO was indicated in Scheme 1. Under visible light, in the valence band (VB) of $NiFe_2O_4$ will be induced to the CB and then photogenerated electrons can migrated TA and ZnO. The reason why excited electrons are transferred from the CB potential of $NiFe_2O_4$ to the CB potential of ZnO, the CB potential of $NiFe_2O_4$ is more negative (-0.60 eV) than that of the ZnO (-0.12 eV). Similarly, the VB potential of $NiFe_2O_4$ (1.00 eV) is more negative than that of the ZnO (3.00 eV). So, the photogenerated electrons in $NiFe_2O_4$ are flown to TA and ZnO. In the meantime, the photogenerated holes are transferred from ZnO to $NiFe_2O_4$ [4,19]. The adsorbed oxygen molecules serve as the electron trapping to produce superoxide radicals. The holes will interact with H_2O to fabricated hydroxyl radicals. As a result, these strong radicals will attack to the CR and degrade to carbondioxide and water [4,13,19]. The proposal degradation mechanism of CR is demosntrated as follows:

$$NiFe_2O_4+hv \xrightarrow{\text{visible light}} NiFe_2O_4(h^+)+ZnO(e^-) \quad (1)$$

$$ZnO\ (e^-) + TA \xrightarrow{\text{visible light}} ZnO + TA\ (e^-) \quad (2)$$

$$e^- + O_2 \rightarrow \bullet O_2^- \quad (3)$$

$$\bullet O_2^- + H^+ + e^- \rightarrow \bullet OH + OH^- \quad (4)$$

$$h^+ + H_2O \rightarrow \bullet OH + H^+ \quad (5)$$

$$\bullet OH/h^+ + \text{dye} \rightarrow \text{degradation products} \quad (6)$$

Consequently, the enhanced photocatalytic efficiency of $NiFe_2O_4$, with the deposition of TA and ZnO may be clarified in three paths: (1) accelerating the separation of charge carriers, (2) improving the specific surface field, and (3) advancing the visible light usage capacity.

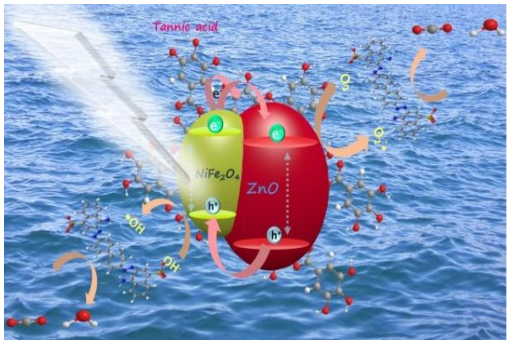

Scheme 1. Schematic representation of photocatalytic degradation for CR via $NiFe_2O_4$/TA/ZnO.

4. Conclusions

In conclusion, a magnetically separable $NiFe_2O_4$, $NiFe_2O_4$/TA and $NiFe_2O_4$/TA/ZnO were prepared by solvothermal method. $NiFe_2O_4$/TA/ZnO nanocomposites

exhibited advanced photocatalytic performance compared to the other photocatalyts. The advanced photocatalytic efficiency is related to the synergistic relationship between $NiFe_2O_4$, ZnO and TA. The narrow band gap energy and magnetically separable of $NiFe_2O_4$ and the enhanced electron transfer capability of TA positively impressed photodegradation process. It is hoped that the $NiFe_2O_4$/TA/ZnO will be an ideal photocatalyst for decomposition of contaminants with visible light.

Acknowledgments

I would like to thank Prof. Dr. Mahmut Özacar and Dr. Nuray Güy for helping this study.

References

1. Alam, U, Khan, A, Raza, W, Khan, A, Bahnemann, D, Muneer, M, Highly efficient Y and V co-doped ZnO photocatalyst with enhanced dye sensitized visible light photocatalytic activity, *Catalysis Today*, 2017, 284, 169–178.

2. Lin, X, Chen, H, Hu, Z, Hou, Y, Dai, W, Enhanced visible light photocatalysis of TiO_2 by Co-modification with Eu and Au nanoparticles, *Solid State Science*, 2018, 83, 181–187.

3. Adeleke, J.T, Theivasanthi, T, Thiruppathi, M, Swaminathan, M, Akomolafe, T, Alabi, A.B, Photocatalytic degradation of methylene blue by ZnO/$NiFe_2O_4$ nanoparticles, *Appied Surface Science*, 2018, 455, 195–200.

4. Ren, A, Liu, C, Hong, Y, Shi, W, Lin, S, Li, P, Enhanced visible-light-driven photocatalytic activity for antibiotic degradation using magnetic $NiFe_2O_4$/Bi_2O_3 heterostructures, *Chemical Engineering Journal*, 2014, 258, 301–308.

5. Pant, B, Park, M, Kim, H.Y, Park, S.J, Ag-ZnO photocatalyst anchored on carbon nanofibers: Synthesis, characterization, and photocatalytic activities, *Synthetic Metals*, 2016, 220, 533–537.

6. Delsouz, Khak, M.R, Shafeeyan, M.S, Raman, A.A.A, Daud W.M.A.W, Evaluating the efficiency of nano-sized Cu doped TiO_2/ZnO photocatalyst under visible light irradiation, *Journal of Molecular Liquids*, 2018, 258, 354–365.

7. Davar, N, Farhadian, M, Nazar, A.R.S, Homayoonfal M., Degradation of diphenhydramine by the photocatalysts of ZnO/Fe_2O_3 and TiO_2/Fe_2O_3 based on clinoptilolite: Structural and operational comparison, *Journal of Environmental Chemical Engineering*, 2017, 5, 5707–5720.

8. Zeng, J, Song, T, Lv, M, Wang, T, Qin, J, H, Zeng, Plasmonic photocatalyst Au/g-C_3N_4/$NiFe_2O_4$ nanocomposites for enhanced visible-light-driven photocatalytic hydrogen evolution, *RSC Advances*, 2016, 6, 54964–54975.

9. Sun, J, Fu, Y, Xiong, P, Sun, X, Xu, B, Wang, X, A magnetically separable P25/$CoFe_2O_4$/graphene catalyst with enhanced adsorption capacity and visible-light-driven photocatalytic activity, *RSC Advances*, 2013, 3, 22490.

10. Xia,Y, He, Z, Su, J, Tang, B, Hu, K, Lu, Y, Sun, S, Li, X, Fabrication of magnetically separable $NiFe_2O_4$/BiOI nanocomposites with enhanced photocatalytic performance under visible-light irradiation, *RSC Advances*, 2018, 8, 4284–4294.

11. Patil, S.S, Tamboli, M,S, Deonikar, V.G, Umarji, G.G, Ambekar, J.D., Kulkarni, M.V., Kolekar S.S., Kale, B.B., Patil, D.R., Magnetically separable Ag_3PO_4/$NiFe_2O_4$ composites with enhanced photocatalytic activity, *Dalton Transactions*, 2015, 44, 20426–20434.

12. Çakar, S, Özacar, M, Fe–tannic acid complex dye as photo sensitizer for different morphological ZnO based DSSCs, *Spectrochimica Acta Part A Molecular and Biomolecular Spectroscopy*, 2016, 163, 79–88.

13. Güy, N, Özacar, M, Visible light-induced degradation of indigo carmine over $ZnFe_2O_4$/Tannin/ZnO: Role of tannin as a modifier and its degradation mechanism, *International Journal of Hydrogen Energy*, 2018, 43, 8779–8793.

14. Güy, N, Çakar, S, Özacar, M, Comparison of palladium/zinc oxide photocatalysts prepared by different palladium doping methods for congo red degradation, *Journal of Colloid and Interface Science*, 2016, 466, 128–137.

15. Güy, N, Atacan, K, Karaca, E., Özacar, M, Role of Ag_3PO_4 and Fe_3O_4 on the photocatalytic performance of magnetic Ag_3PO_4/ZnO/Fe_3O_4 nanocomposite under visible light irradiation, *Solar Energy*, 2018, 166, 308–316.

16. Atacan, K, Özacar, M, Özacar, M, Investigation of antibacterial properties of novel papain immobilized on tannic acid modified Ag/$CuFe_2O_4$ magnetic nanoparticles, *International Journal of Biolological Macromolecules*, 2018, 109, 720–731.

17. Şen, Türkyılmaz, Ş, Güy, N, Özacar, M, Photocatalytic efficiencies of Ni, Mn, Fe and Ag doped ZnO nanostructures synthesized by hydrothermal method: The synergistic/antagonistic effect between ZnO and metals, *Journal of Photochemistry and Photobiology A: Chemistry*, 2017, 341, 39–50.

18. Güy, N, Özacar, M, The influence of noble metals on photocatalytic activity of ZnO for Congo red degradation, *International Journal of Hydrogen Energy*, 41 (2016) 20100–20112.

19. Zhu, H,Y, Jiang, R, Fu Y.Q, Li, R.R, Yao, J, Jiang, S.T, Novel multifunctional $NiFe_2O_4$/ZnO hybrids for dye removal by adsorption, photocatalysis and magnetic separation, *Applied Surace Science*, 2016, 369, 1–10.

20. Gautam, S, Shandilya, P, Singh, V.P, Raizada, P, Singh, P, Solar photocatalytic mineralization of antibiotics using magnetically separable $NiFe_2O_4$ supported onto graphene sand composite and bentonite, *Journal of Water Process Engineering*, 2016, 14, 86–100.